Spin waves in ultrathin hexagonal cobalt films on W(110), Cu(111), and Au(111) surfaces

E. Michel,[1,3] H. Ibach,[2,3,*] and C. M. Schneider[1,3]
[1]*Peter Grünberg Institut (PGI-6), Forschungszentrum Jülich, 52425 Jülich, Germany*
[2]*Peter Grünberg Institut (PGI-3), Forschungszentrum Jülich, 52425 Jülich, Germany*
[3]*Jülich Aachen Research Alliance, Germany*
(Received 19 January 2015; revised manuscript received 28 April 2015; published 8 July 2015)

Spin wave spectra of ultrathin epitaxial cobalt films deposited on W(110), Cu(111), and Au(111) surfaces are studied in the wave-vector regime between 0.1 Å^{-1} and 0.7 Å^{-1} using inelastic electron scattering with 6 meV energy resolution. Up to three different spin wave modes are resolved for wave vectors $q_\parallel < 0.35\ \text{Å}^{-1}$. The modes are identified as the acoustic mode and standing modes with one and two nodes inside the film. The relative weight of the modes in a particular spectrum may depend critically on the electron impact energy. For larger wave vectors beyond $q_\parallel > 0.35\ \text{Å}^{-1}$ and layers thicker than five atom layers the separate modes merge into a single, broad loss feature. Since the shape and position of the loss feature depend on the electron impact energy, a separation into different modes is nevertheless possible for not too large wave vectors. The spin wave dispersion curves of films grown on W(110) agree with those observed on Cu(111) if one takes into account that on copper the cobalt grows in islands so that the mean height of the islands is higher than the nominal coverage. On films grown on Au(111) the low wave vector spin waves are buried in the high elastic diffuse scattering caused by the considerable disorder in the films. The broader appearance of the spectra at higher wave vectors compared to films grown on W(110) and Cu(111) is quantitatively accounted for by disorder-induced kinematic broadening. Because of the granular growth on copper and gold primarily the spin wave spectrum of cobalt films on W(110) is amenable to quantitative theoretical analysis. Such an analysis is not available at present. We show however, that the dispersion curves are incompatible with the Heisenberg model as long as only a single, layer-independent exchange coupling constant is invoked.

DOI: 10.1103/PhysRevB.92.024407 PACS number(s): 75.70.Tj, 75.30.Ds

I. INTRODUCTION

The magnetism of thin films is a fascinating and rich field of contemporary research, partly because of its technological importance, and partly because of the scientific challenges involved in our fundamental understanding of magnetism. While early research was concerned with the investigation of static magnetic properties such as the orientation of the easy axis of magnetization, the magnetization hysteresis, and the nature of domain walls [1–5], recent studies focus on the dynamics of spin systems. This paper deals with spin dynamics in the form of spin waves. The excitation of a quantum of a spin wave corresponds to the flip of one spin from the majority to the minority state. Spin waves therefore offer the intellectually appealing possibility to transport spin-encoded information in space without transport of charge or mass by forming wave packets of spin waves. In this context the exchange-dominated high wave vector spin waves of 3*d* ferromagnets are of particular interest since they combine high speeds of propagation with the possibility of localization in the nm range. In 1967 Mills proposed to study such high-momentum spin waves at surfaces and in thin films by using inelastic scattering of low-energy electrons [6]. While the experimental techniques for such studies were at hand in the 1970s [7] it took several decades before specifically designed electron spectrometers of sufficient sensitivity became available [8]. Using such an instrument Vollmer *et al.* performed the first study of spin waves in the high-momentum regime on an eight atom layer film of cobalt on a Cu(100) substrate [9]. However, due to the comparatively poor energy resolution only a single broad loss feature was observed as a function of the wave vector parallel to the surface $q_\parallel$ and was attributed to the lowest mode, the surface mode of the film. In analogy to phonon excitations the mode is also called the acoustic mode since (in absence of external magnetic fields or magnetic anisotropies) the frequency becomes zero together with the wave vector parallel to the surface $q_\parallel$. The reason is that for $q_\parallel = 0$ all spins in the film precess in phase. The torque on the spins therefore vanishes. For small $q_\parallel$ and thin films, amplitude and phase of the acoustic mode are (nearly) the same in all layers of the film. In that sense the mode may be also called the homogeneous mode. However, for large $q_\parallel$ near the boundary of the surface Brillouin zone the mode becomes localized either to the surface or to the interface, depending on the layer dependence of the exchange interaction [10]. Simultaneously, the spin wave excitations become extremely broad in energy since they rapidly decompose into Stoner excitations in 3*d* metals. The energy width of the spin wave excitations is then of the same magnitude as the energy itself and the various modes of the film merge into a broad, rather featureless response function [11]. A dispersion of an individual mode is not definable then.

For smaller wave vectors $q_\parallel < 0.3$–$0.4\ \text{Å}^{-1}$, however, spin waves are well-defined excitations, even in 3*d* metals. This work therefore focuses on the low wave vector regime. The spin wave spectrum of a film then consists of a series of modes displaying an individual dispersion with $q_\parallel$. The total number of dispersion branches (with the acoustic mode included) equals the number N of atom layers in the film. The higher frequency modes of the film are standing wave modes along the vertical axis of the film with 1 to N–1 nodes inside

*corresponding author: h.ibach@fz-juelich.de

the film. These standing modes were not explicitly seen in the early studies using electron energy loss spectroscopy [9,12–15] although they were known to exist at $q_{\parallel} = 0$ from spin polarized scanning tunneling spectroscopy [16–19]. By using an improved electron spectrometer [20,21] with five times higher energy resolution the lowest standing mode of a cobalt film was discovered for $q_{\parallel} < 0.4^{-1}$ [22]. A systematic analysis of the spin wave spectrum of fcc cobalt films deposited on Cu(100) as function of the layer thickness (5–8 atom layers) [23] in connection with theoretical calculations of the exchange coupling constants [24] has led to a new interpretation of the spin wave spectra at higher wave vectors [10] (near the boundary of the surface Brillouin zone), namely that the spectra consist of several modes, which cannot be disentangled as the energy differences between the various losses are smaller than the intrinsic width of the losses. A simulation of the spin wave spectrum by invoking a simple model for the scattering cross section revealed that at larger wave vectors $q_{\parallel}$ the spin wave signal of the system Co/Cu(100) is actually dominated by the first standing mode and not by the lowest mode as originally assumed [9]. It has thereby become clear that the assignment of the position of a broad spin wave signal to a single mode and the discussion of the dispersion of that peak position in terms of theory is questionable except for the case of magnetic monolayers or bilayers (for a review see Ref. [25]). As will be shown in this paper the situation is even more complicated by the fact that the relative weight of an individual mode to a spin wave signal can depend very critically on the electron impact energy. For larger wave vectors, where the energy difference between modes is smaller than their energy width the shape of the spin wave signal varies with the impact energy. A shift in the maximum of the spin wave signal as function of film thickness [26] is therefore not necessarily due to variations of intrinsic magnetic properties.

The simultaneous observation of the acoustic mode and one or more standing modes and their dispersion as function of the film thickness provides information on the layer dependence of the exchange coupling. For example, the energy of a standing spin wave at $q_{\parallel} = 0$ is determined solely by the interlayer coupling. The thinner the film, the larger is the contribution of the interlayer coupling between layers next to the interface and the surface. The standing wave energies as a function of the layer thickness therefore reveal the layer dependence of the interlayer coupling. The dispersion with the wave vector parallel to the surface is governed by the intralayer coupling. Consequently one may learn about intralayer coupling from the dispersion with $q_{\parallel}$. Again, the role of surface and interface layers increases with decreasing film thickness. A systematic experimental study of the dispersion of acoustic and standing spin wave modes as a function of the layer thickness should therefore reveal information on the layer dependence of intralayer and interlayer exchange coupling parameters. However, the experimental data cannot be interpreted without the help of theory. The reason is the presence of two surfaces, the free surface and the interface to the substrate. Theory has shown that the exchange coupling constants at surface and interface differ considerably from each other [24,27]. A complete experimental data set on the spin waves as function of thickness may therefore indicate substantial surface/interface modifications of the exchange coupling, but there is no way to determine the share of either surface in these modifications unless one is guided by theory. For fcc cobalt layers on Cu(100) [23] guidance by theory was available [24,27] and excellent agreement between experimental dispersion data and those calculated from the (slightly reduced) exchange coupling constants of Bergqvist *et al.* [24] was found.

It is the prime objective of this paper to extend the concept for the analysis of the layer dependence of the exchange coupling to hexagonal (hcp) cobalt films with (0001) surfaces. For these films, one expects a considerable reduction of the energies of standing waves in (0001) oriented hexagonal films [and (111) oriented fcc films] since the number of nearest neighbors mediating the interlayer coupling is lower compared to fcc (100) films. On the other hand, the intralayer coupling involves six instead of four nearest neighbors. For the same reason the modifications of the intralayer and interlayer exchange coupling near the surface and the interface are expected to be quite different from fcc (100) films.

For the type of study that we have in mind one needs an epitaxial system in which cobalt grows in well-ordered hcp films in a layerwise growth mode so that a particular dispersion of a standing wave can be attributed to a defined layer thickness. Such well-ordered hcp cobalt films with comparatively little strain grow on W(110) [28,29]. The rather perfect order of these films results in small elastic diffuse scattering. Consequently, low-energy spin waves can be observed even for small wave vectors as their loss features are not buried in the elastic diffuse scattering. Unfortunately, the hexagonal cobalt lattice is incommensurate with the substrate lattice. A theoretical analysis therefore requires the handling of a large unit cell. We therefore decided to explore also the spin wave spectra of hexagonal films as realized by deposition onto Cu(111) and Au(111) where the unit cell is (1×1). However, in both cases the growth is not layer by layer but rather in the form of islands created in the initial nucleation process.

On Cu(111), cobalt nucleates in two-layer-high islands, which assume a triangular shape in room-temperature growth. The shape arises from the fact that (100) boundaries of the cobalt double layers disappear during growth [30]. Since the first layer cobalt atoms occupy A sites or B sites of the Cu(111) surface with equal probability the islands possess two different orientations rotated by 60° with respect to each other [31]. In other words, the islands grow in twins. The structure, the electronic properties and the magnetism of these nanoislands have attracted considerable attention in the past [32–35]. An earlier proposition that the two-layer-high islands actually consist of cobalt trilayers with the bottom layer embedded into the copper matrix [36] are not confirmed by these recent studies. Upon further deposition of cobalt the islands grow in size and thickness, initially retaining the fcc structure of the substrate. The LEED pattern nevertheless displays sixfold symmetry because of the two types of islands, which are rotated by 60° with respect to each other. Again because of the twin structure the islands do not merge into a continuous film during further growth. Even a five-monolayer (5ML) film shows remnants of the original islands with deep trenches between them. According to a LEED analysis the structure of the cobalt layer is then predominantly hcp [37,38]. Despite their granular structure these cobalt films display well-defined spin wave spectra,

equally rich in features as the hcp films on W(110), as we shall see. The reason is that the islands have a mesalike shape with a rather uniform height. The thickness of the film within the islands is not known *a priori* but must be larger than the mean thickness. A theoretical analysis of the spectra must therefore involve a calibration of the actual height of the islands. Since the energy of the standing spin wave modes depends critically on the number of layers in the film an approximate calibration can be achieved by the comparison of the standing spin waves of cobalt films deposited on W(110) and Cu(111).

For the sake of completeness we also consider the spin wave spectra of hcp cobalt films grown on Au(111). These films are the least ordered ones in our study. The disorder stems from the large mismatch between the Au(111) surface lattice constant ($a = 2.88$ Å) and hcp cobalt ($a = 2.51$ Å) as well as from the nucleation in specific sites of the reconstructed surface. The cobalt films therefore have a pronounced granular structure [39], which persists up to thicker layers. Nevertheless cobalt films on Au(111) have been of interest because of a reorientation transition between four- and five-monolayer thickness in which the magnetization switches from vertical polarization caused by a large interface anisotropy to parallel orientation [40–42]. The large interface anisotropy has also been studied on Au/Co multilayer systems [43,44].

The paper is organized as follows. The next section introduces details of our experimental setup, describes the cleaning procedures, the thickness calibration, as well as some technicalities of the data analysis. Sections III–V are devoted to the experimental results for cobalt films on W(110), Cu(111), and Au(111), respectively. The final section discusses effects of the film morphology and compares the dispersion curves of acoustic and standing modes obtained for hcp films to those of the fcc cobalt films on Cu(100). Contrary to expectation, we find the standing modes of the hcp (0001) films to be of nearly the same frequency. We argue that the reason for the unexpectedly high energies of the standing modes is the higher contribution of next-nearest-neighbor interactions.

II. EXPERIMENT

Our experimental setup features a preparation chamber equipped with means for LEED (low-energy electron diffraction) and a cylindrical mirror Auger analyzer. The LEED system is in line of sight with the electron gun of the Auger analyzer, which permits grazing incidence electron diffraction studies during deposition of the cobalt films. Calibration of the e-beam evaporator in terms of the ion flux associated with the cobalt evaporation is made via the oscillations in the intensity of the (00) diffracted 3 keV grazing incidence beam (MEED oscillations) during the layer-by-layer growth of cobalt on a Cu(100) crystal. By scaling with the atom layer density the film thickness is then calibrated for other surface orientations. The copper and gold surfaces were cleaned by argon sputtering and annealing in the conventional way. The tungsten surfaces are prepared firstly by cycles of oxygen treatment (3×10^{-7} mbar O_2 pressure) at 1600 K sample temperature followed by flashing the crystal to 2300 K. This procedure leaches the carbon out of the crystal. Once the bulk of the crystal is sufficiently depleted of carbon, merely flashing to 2300 K in ultrahigh vacuum (base pressure in the low 10^{-11} mbar range) suffices to remove impurities as well as cobalt layers from earlier deposition. All stages of the cleaning and preparation procedure were monitored via the vibration spectrum of adsorbed species using our electron energy loss spectrometer. The sensitivity of this spectroscopy is about a hundred times higher than Auger spectroscopy as will be demonstrated below.

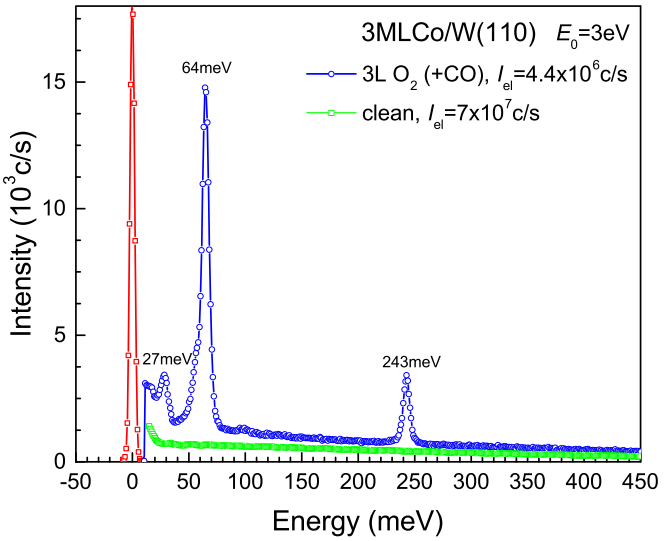

FIG. 1. (Color online) Energy loss spectrum for about a monolayer of oxygen (64 meV) with some additional CO contamination (243 meV) on a three monolayer cobalt film deposited on W(110) (blue circles). The oxygen contamination level of the clean surface is less than 10^{-4} of a monolayer (see text for discussion).

Our electron energy loss spectrometer is housed in a separate chamber into which the samples are transferred after preparation. The spectrometer features a conventional LaB_6 cathode as electron source and two 143° electrostatic deflectors as monochromators and analyzers each. The present instrument is equipped with a new (more compact) cathode emission system yielding about six times higher monochromatic currents compared to the instrument described in Refs. [10,21]. Because of the conventional cathode, spin wave excitations are identified solely by their dispersion characteristics. Since spin wave energy losses are energetically broader and more than an order of magnitude weaker than vibration energy losses of surface contaminations, extreme cleanliness of the surface down to a level $<10^{-2}$ of a monolayer is needed. Much more care in surface and film preparation is therefore required compared to spectroscopy involving a spin polarizing cathode where vibration peaks of the same order of magnitude as the spin wave loss were frequently tolerated in the past (see e.g., Refs. [13,26]). Figure 1 demonstrates that the required low contamination level can indeed be achieved. The figure shows the specular-reflection spectrum of a clean three-monolayer (3ML) cobalt film deposited on W(110) (green open squares) in comparison to the spectrum of about a monolayer of oxygen with some additional CO contamination. The elastic line (red squares in Fig. 1) is recorded with reduced voltage on the channeltron detector and therefore not calibrated in height. The true elastic intensity was determined by measuring the current at the channeltron entrance using a pA meter. The

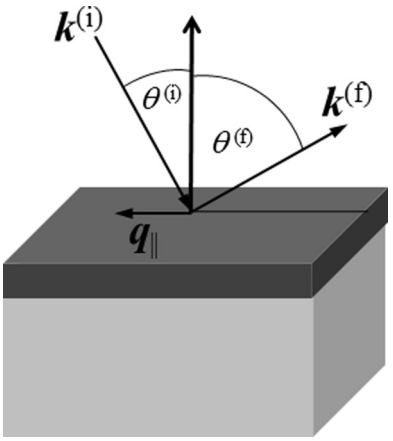

FIG. 2. Schematic illustration of the scattering geometry.

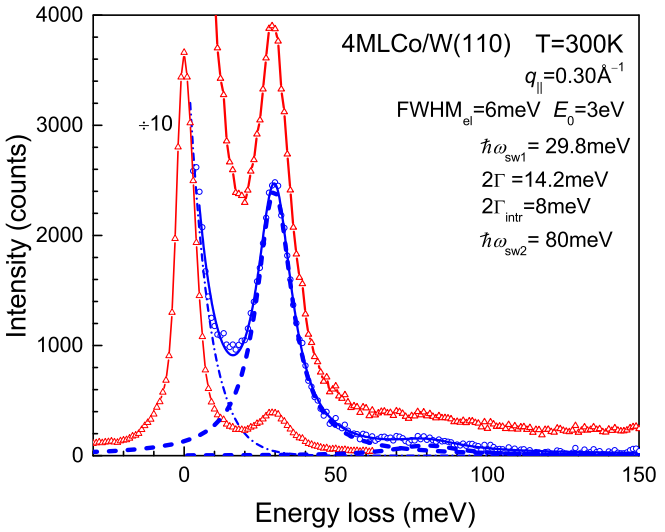

FIG. 3. (Color online) Energy loss spectrum of a four monolayer (4ML) cobalt film deposited on a W(110) surface. The energy losses correspond to the acoustic spin wave at $E_{\mathrm{sw1}} = 29.8$ meV and the first standing spin wave at $E_{\mathrm{sw2}} = 80$ meV. The wave vector is $q_{\parallel} = 0.3$ Å^{-1}. See text for further details.

measured current corresponds to 4.4×10^6 electrons/s and 7×10^7 electrons/s, for the oxygen covered surfaces and the clean surface respectively. For the clean surface, the intensity of the oxygen mode is below 20 counts/s compared to 1.5×10^4 counts/s for the surface with one monolayer of oxygen. Since for a given coverage the intensity of a vibration peak in the dipole scattering regime [7] is proportional to the elastic intensity one calculates the oxygen contamination level of the clean surface to $(20/7 \times 10^7)/(1.5 \times 10^4/4.4 \times 10^6) = 8 \times 10^{-5}$. A similar result applies to the carbon contamination.

The determination of the spin wave dispersion requires an accurate knowledge of the kinetic energy E_0 of electrons at the sample. The energy is established in two steps. First, the pass energy E_{pass} in the monochromator is calculated from the deflection voltage [20]. The kinetic energy is then given by

$$E_0 = E_{\mathrm{pass}} + e\Delta V + e(\Phi_{\mathrm{graphite}} - \Phi_{\mathrm{sample}}) \qquad (1)$$

in which ΔV is the voltage difference between the exit of the monochromator and the sample and $e(\Phi_{\mathrm{graphite}} - \Phi_{\mathrm{sample}})$ is the work function difference between the graphite-coated exit slit of the monochromator and the sample. The work function difference is experimentally determined by applying a negative bias on the sample until no current reaches the sample despite refocusing the lenses. This determines the voltage of zero kinetic energy of electrons at the sample. The difference between that bias voltage and the voltage applied in the experiment defines the electron impact energy.

A schematic illustration of the scattering geometry used in the measurements is shown in Fig. 2. An incident electron beam at angle $\theta^{(\mathrm{i})}$ with respect to the surface normal with wave vector $k^{(\mathrm{i})}$ is backscattered from the surface. Some electrons undergo inelastic scattering and thereby transfer energy and momentum. The intensity of the scattered electrons with wave vector $k^{(\mathrm{f})}$ is measured at angle $\theta^{(\mathrm{f})}$. Spin waves appear in the spectrum as energy losses $\hbar\omega_{\mathrm{s}}$ or energy gains. For elementary excitations characterized by the two-dimensional wave vector $q_{\parallel}$ momentum conservation between the incoming and outgoing electrons requires that for energy losses $q_{\parallel}$ is

$$q_{||} = k^{(\mathrm{i})} \sin\left(\theta^{(\mathrm{i})}\right) - k^{(\mathrm{f})} \sin\left(\theta^{(\mathrm{f})}\right) \quad \text{if} \quad E^{(f)} = E^{(i)} - \hbar\omega_s \qquad (2)$$

while for energy gains $q_{\parallel}$ is given by

$$-q_{||} = k^{(\mathrm{i})} \sin\left(\theta^{(\mathrm{i})}\right) - k^{(\mathrm{f})} \sin\left(\theta^{(\mathrm{f})}\right) \quad \text{if} \quad E^{(f)} = E^{(i)} + \hbar\omega_s. \qquad (3)$$

In our experiments, the angle between the incoming beam and the scattered beam is kept constant at 90°, occasionally at 80°. The required parallel wave vector transfer is achieved by rotating the sample around an axis vertical to the scattering plane. For the impact energies E_0 used here, the accuracy in the determination of $q_{\parallel}$ is 0.004 Å^{-1}. All spectra are recorded with $\theta^{(i)} < \theta^{(f)}$ that is for $q_{\parallel} < 0$. The area on the surface, which is probed by the analyzer is then larger than the area illuminated by the electron beam, which leads to higher intensities than in the reverse case. Since the hexagonal films have a center of inversion Dzyaloshinskii-Moriya interactions [45] do not play a role in this case (as opposed to the case of iron bilayer films on the same surface [46,47]) and the dispersion is the same for positive and negative $q_{\parallel}$. In the following we therefore quote only the modulus $q_{\parallel}$.

In order to illustrate the procedures for data analysis, the energy loss spectrum of a 4ML cobalt film on W(110) is shown in Fig. 3. The spectrum displays the energy losses due to the acoustic spin wave mode at $\hbar\omega_{\mathrm{sw1}} = 29.8$ meV and due to the lowest standing spin wave at $\hbar\omega_{\mathrm{sw2}} = 80$ meV. Electron impact energy is 3 eV, the $q_{\parallel}$ vector is 0.3 Å^{-1} [before correction for the energy loss dependent value of k^f]. Energy losses scale with $n(\hbar\omega, T) + 1$ where n is the Bose occupation number. The true spectral density is therefore recovered from the spectrum by dividing the energy loss spectrum (red triangles in Fig. 3) by $n(\hbar\omega, T) + 1$. The result is the curve with blue open circles. Spin wave excitations possess a Lorentzian line shape [11,48]. The spectrometer energy-transfer function as represented by the elastic line in the spectrum is approximately a Gaussian. The spectral response

of a spin wave is therefore a convolution of a Gaussian with a Lorentzian, a Voigt function. Since the energy width of the elastic peak is narrower than the spin wave signal the spin wave loss is nevertheless well represented by a Lorentzian. The spectral density is therefore analyzed by fitting a tail of the elastic diffuse scattering, two Lorentzians, and a constant background to the experimental spectral density (blue solid line). Tail and Lorentzians are shown as dash-dotted and dashed lines in Fig. 3. The fitting procedure yields a full width at half maximum (FWHM) of $2\Gamma = 14.2$ meV for the lowest spin wave. A detailed study of the FWHM of acoustic spin waves of the hcp films with 3 meV energy resolution is a subject for future research [49]. Here we merely note that the intrinsic FWHM of the acoustic spin wave signal after correction for energy and momentum resolution [22] is about $2\Gamma_{\text{intr}} = 8$ meV. Acoustic spin waves in hexagonal cobalt films on W(110) are therefore well-defined excitations.

III. COBALT LAYERS ON W(110)

Cobalt films on W(110) grow in the Nishiyama-Wassermann orientation, that is with the hexagonal base plane parallel to the W(110) plane. The cobalt $[11\bar{2}0]$ and $[1\bar{1}00]$ directions are parallel to the W[001] and W$[1\bar{1}0]$ directions, respectively. The cobalt films grow pseudomorphic along the W$[1\bar{1}0]$ direction so that the hexagonal cobalt film is slightly strained in that direction. A detailed study of the strain as a function of the film thickness was performed by Fritzsche *et al.* [28]. Along the W[001] direction, the mismatch of the lattice constants causes a misfit $f = (a_{\text{Co}} - a_{\text{W}})/a_{\text{W}} = -0.208$ which gives rise to a characteristic superstructure in the LEED pattern [Fig. 4(a)] as long as the film thickness is sufficiently small so that electrons can penetrate down to the tungsten substrate. For films between 2ML and 8ML the lattice constants derived from the LEED spots are in a ratio of 3.56:4.56 = 0.781 [28,50], which lies between the commensurate ratios 3:4 and 4:5. A real space structure with the closest commensurate ratio 4:5 leading to a 4×1 unit cell is illustrated in Fig. 4(b) with a single layer of cobalt atoms.

Spin wave spectra are studied with the wave vector $q_{\parallel}$ along the Co$[11\bar{2}0]$ direction, which is the $\bar{\Gamma}\ \bar{K}$ direction in the surface Brillouin zone of the hexagonal cobalt lattice (Fig. 5). Examples for Co/W(110) are shown in Fig. 6 for a wave vector $q_{\parallel} = 0.3\,\text{Å}^{-1}$ and film thicknesses between 3ML and 7ML. The spectra display up to four loss features. The lowest one at 18 meV is a phonon resonance loss due to a high density of bulk states [51] (see Supplemental Material [52]). The other energy losses are caused by spin wave excitations. The lowest of those is the acoustic mode, which is practically independent of the film thickness.

The next higher mode is the standing mode with one node inside the film. Its energy depends critically on the film thickness. For 6ML and 7ML one notices a further broad feature at higher energies. A systematic study of its peak energy as a function of wave vector identifies the feature as the second standing wave with two nodes inside the film. We note that the spectra show defined standing modes for each of the nominal layer thicknesses (except for 3ML). The FWHM of the standing mode signal is not broader than the FWHM for the acoustic mode at the same spin wave energy.

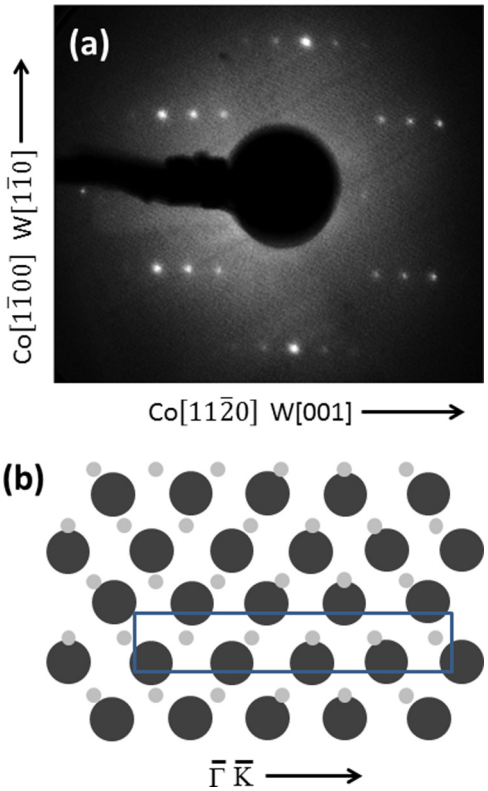

FIG. 4. (Color online) (a) LEED pattern of a 4ML cobalt film on a W(110) surface. Electron energy is 200 eV. The superstructure is caused by the misfit along the W[001] direction. (b) real-space illustration of the W(110) surface (large black spheres) and a single layer of cobalt (small gray spheres). Shown is a 4×1 unit cell, however, the real structure is incommensurate along the W[001] direction.

This entails that the majority of the film must have the same thickness with only small contributions from areas of higher or lower thickness. This result is at variance with the low-energy electron microscopy (LEEM) images published by Duden *et al.* where a 5ML LEEM image displayed areas of 4ML and 6ML coverage of roughly the same size [53].

The absolute intensities as well as the relative intensities of the various modes depend critically on the impact energy. This is illustrated with Fig. 7. Whereas the acoustic spin wave mode (denoted as SW1 in Fig. 7) is hardly discernable at $E_0 = 3$ eV impact energy, it becomes the strongest mode in the spectrum when $E_0 = 2.25$ eV. The same behavior is found for 6ML and

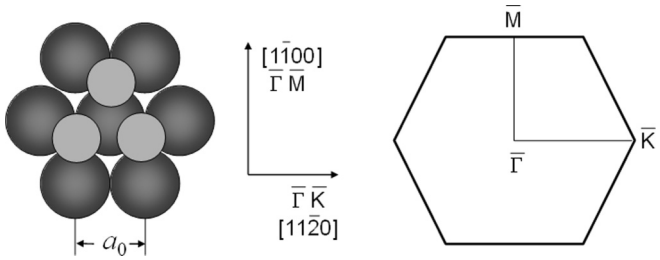

FIG. 5. Two layers of a hexagonal lattice, the principal directions and the surface Brillouin zone.

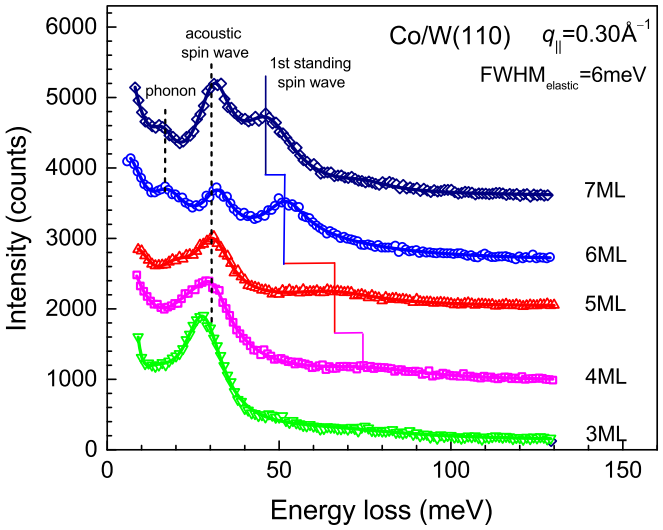

FIG. 6. (Color online) Energy loss spectra for 3–7ML cobalt films at $q_{\parallel} = 0.3\,\text{Å}^{-1}$. The impact energy was 3 eV for 2–6ML and 2.25 eV for 7ML. The lowest spin wave mode at 30 meV is independent of the film thickness. It is therefore assigned to the acoustic mode. The other losses are due to standing spin waves.

8ML films. Similar oscillations, although not as pronounced as here, were seen on fcc cobalt films on Cu(100) surfaces [54]. In analogy to the same phenomenon in phonon losses in the low impact energy range we attribute these oscillations to image potential induced resonances [55]. Large oscillations in the intensity of phonon modes were also reported for higher impact energies. There, the oscillations are attributed to the multiple scattering of electrons [56,57].

While a quantitative theory for the case of spin waves is still lacking, the effect may be exploited to separate different modes even when they cannot be resolved as separate modes because of limited energy resolution or because of the intrinsic

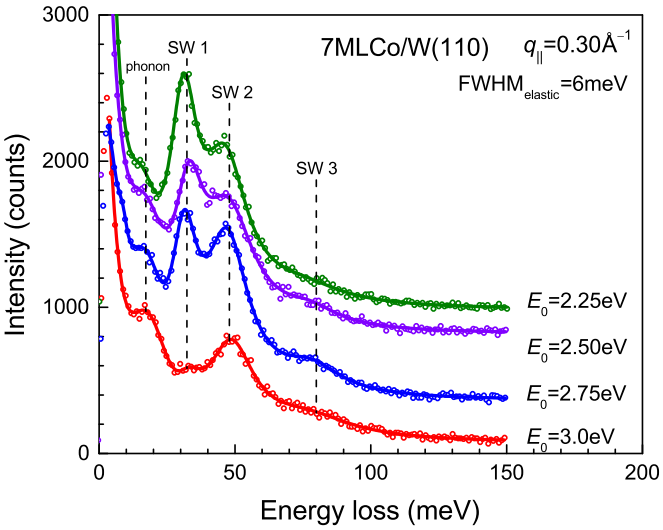

FIG. 7. (Color online) Energy loss spectra as function of the electron impact energy for a 7ML cobalt film at $q_{\parallel} = 0.3\,\text{Å}^{-1}$. The absolute as well as the relative intensities of the various spin wave signals depend critically on the impact energy.

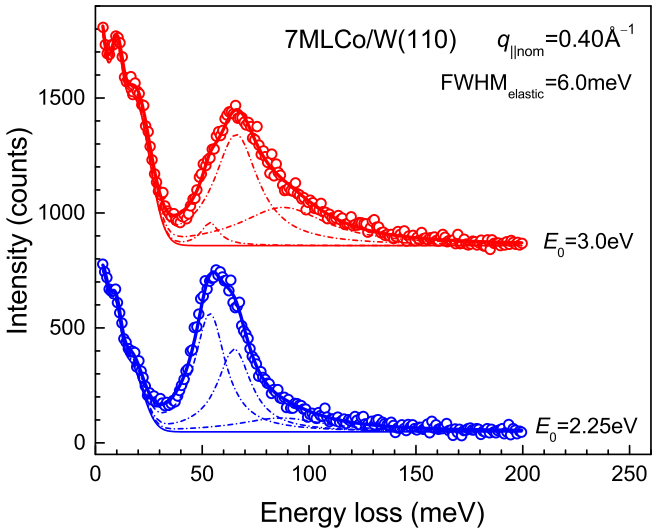

FIG. 8. (Color online) Two energy loss spectra for a 7ML cobalt film at $q_{\parallel} = 0.4\,\text{Å}^{-1}$ taken with two different electron impact energies, 2.25 eV and 3.0 eV.

width of the modes [58,59]. Figure 8 illustrates the method for a 7ML cobalt film: The spin wave signals for $E_0 = 2.25$ eV and $E_0 = 3.0$ eV have a rather different shape and the signals peak at different energies. The spin wave signal is decomposed into Lorentzians at 54 meV, 66 meV, and 88 meV. The precise optimum fit energy for the mode at 66 meV is taken from the $E_0 = 3.0$ eV spectrum since the mode obviously dominates the signal there. The energies for the acoustic mode at 54 meV and the second standing mode at 88 meV are taken from a fit to the $E_0 = 2.25$ eV spectrum. In that way, an unambiguous decomposition into three modes is feasible. We note that the FWHM of the individual contributions to the spin wave signal are 2–3 times smaller than the FWHM of the entire loss peak. Correspondingly, lifetimes of spin waves as taken from the total FWHM [13,60] are short by a factor of 2–3.

The data points on the dispersion of modes, obtained by the procedures described above, are displayed in Fig. 9 for 3ML and 4ML and in Figs. 10(a)–10(c) for 5ML, 6ML, and 7ML, respectively. As previously found for fcc cobalt on Cu(100) [23] the lowest-energy spin wave is practically independent of the film thickness and disperses nearly quadratic in $q_{\parallel}$ for small wave vectors. The next higher-energy branches are standing wave modes with a single node inside the film. Because of the node the energy stays finite for $q_{\parallel} = 0$. For 6ML and 7ML films even a second standing mode (with two nodes) is observed (see also Figs. 6 and 7). The solid, dashed, and dash-dotted lines in Figs. 9 and 10 are fits to guide the eye. The fit function is borrowed from the analytical solution for the acoustic (surface) mode in the nearest-neighbor Heisenberg model. For the basal plane of a hcp structure along the $[11\bar{2}0]$ direction the solution is

$$\hbar\omega_s = \tfrac{16}{3} JS\{3 - \cos(q_{||}a_0) - 2\cos(q_{||}a_0/2)\} \qquad (4)$$

with JS the nearest-neighbor coupling parameter. This analytical solution is a good fit to the peak position of the spin wave loss up to the zone boundary with $JS \sim 14.5$ meV [13]. In order to heuristically describe the standing wave modes the fit

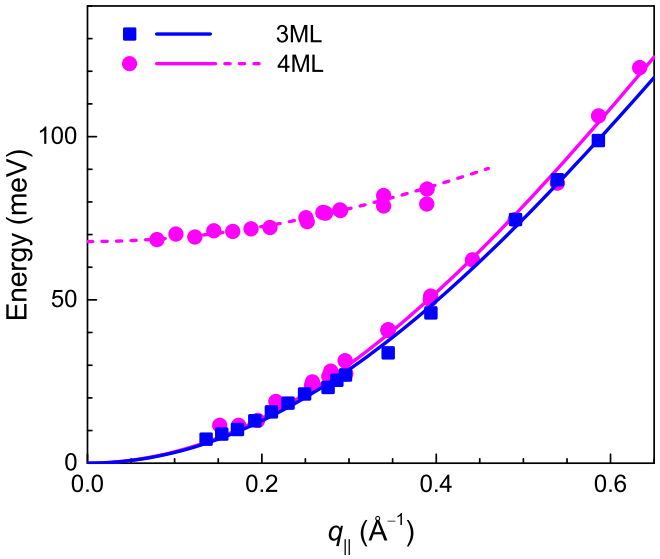

FIG. 9. (Color online) Dispersion of the acoustic and standing wave modes for 3ML and 4ML cobalt films on W(110) (blue solid squares, magenta solid circles, respectively). Solid and dashed lines are fits to guide the eye (see text for discussion).

function is modified to

$$\hbar\omega_s = A\{3 - \cos[(q_{\parallel}^2 + q_{\perp}^2)^{1/2} a_0] - 2\cos[(q_{\parallel}^2 + q_{\perp}^2)^{1/2} a_0/2]\} \quad (5)$$

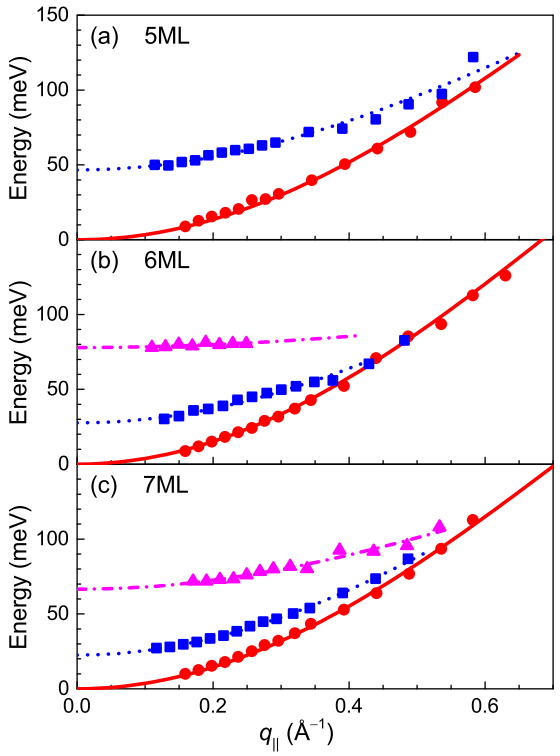

FIG. 10. (Color online) Dispersion of the acoustic and standing wave modes for 5–7ML cobalt films on W(110). Solid and dashed lines are fits to guide the eye (see text for discussion).

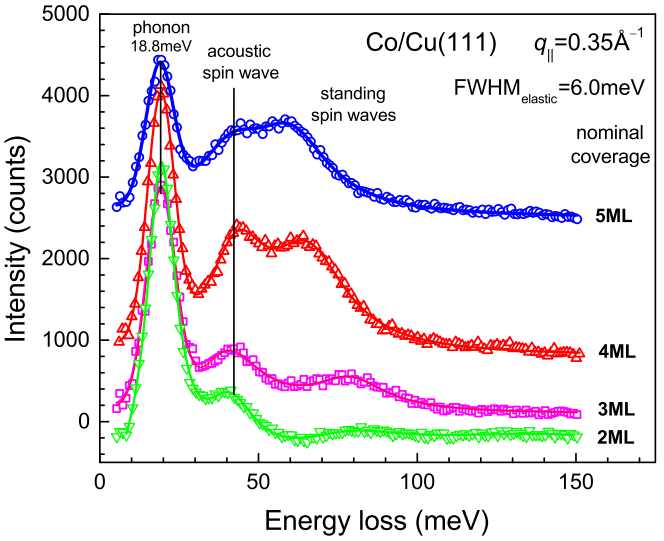

FIG. 11. (Color online) A series of energy loss spectra at wave vector $q_{\parallel} = 0.35$ Å^{-1} as function of the nominal coverage defined as the coverage in layers, which existed if cobalt were to grow as a continuous pseudomorphic film. The peak at 18.8 meV is due to a phonon resonance as discussed before (see also supporting material). The higher-energy losses are due to spin wave excitations as identified by their dispersion.

in which A and $q_{\perp}$ are fit parameters. Only the positions of clearly separate peaks (such as shown in Fig. 6) obtained for wave vectors below $q_{\parallel} = 0.3$–0.4 Å^{-1} are used in the fitting procedure. The extrapolation of the fit functions into the higher $q_{\parallel}$ range beyond 0.4 Å^{-1} nevertheless runs through the data points obtained by the procedure described above, which allows the assignment of these data points to particular dispersion branches (Fig. 10).

IV. COBALT ON Cu(111)

Figure 11 displays a series of energy loss spectra at $q_{\parallel} = 0.35$ Å^{-1} as a function of the nominal coverage defined as the coverage in layers which existed if cobalt were to grow as a continuous pseudomorphic film. The peak at 18.8 meV is due to a phonon resonance as discussed before (see also Supplemental Material [52]). The higher-energy losses are due to spin wave excitations as identified by their dispersion (see below). As in the case of W(110) substrates, the signal, which is largely independent of the film thickness, is the acoustic mode. The thickness-dependent higher-energy mode is a standing wave mode. Because of the aforementioned trenches between the islands the loss spectra may stem from cobalt islands, which are thicker than the nominal coverage. It is therefore *a priori* not possible to associate the standing spin wave signals to a specific film thickness. Here, the comparison to the continuous films on W(110) is helpful. We therefore present the dispersion data for the spin waves of cobalt on Cu(111) together with the data on W(110). Data on the acoustic mode, which are practically independent of the layer thickness, agree within the limits of error, even for the case of 2ML high islands on Cu(111) as obtained with 0.7ML nominal coverage

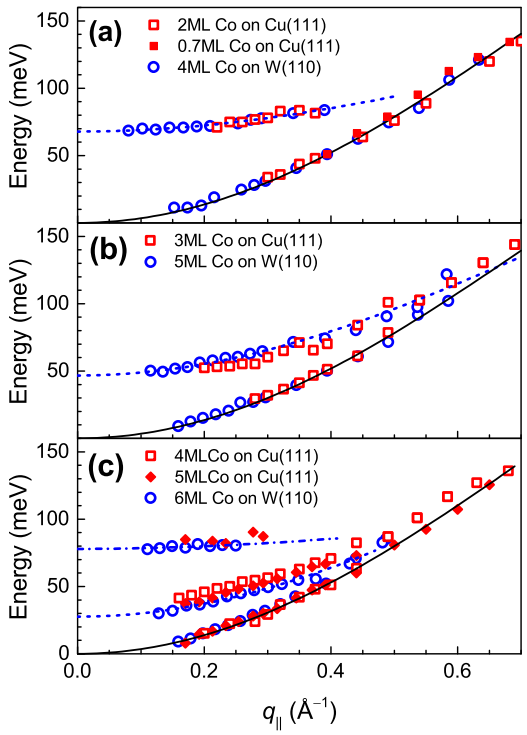

FIG. 12. (Color online) Comparison of the dispersion of spin wave modes of cobalt films grown on Cu(111) to those grown on W(110). (a) 2ML Co/Cu(111), 0.7MLCo/Cu(111), and 4ML Co/W(110) are shown as red open squares, red solid squares, and blue open circles, respectively. (b) 3ML Co/Cu(111) and 5ML Co/W110) are shown as open red squares and open blue circles, respectively. (c) 4ML Co/Cu(111), 5ML Co/Cu(111) and 6ML Co/W(110), are shown as open red squares, solid red diamonds, and open blue circles, respectively. The lines represent fits to the W(110) data using the fit functions described earlier.

[Fig. 12(a)]. The energies of the standing modes, however, disagree with cobalt films of the same nominal thickness on W(110), in particular in case of very thin films. Figure 12(a), e.g., shows that the standing wave data for the 2ML/Cu(111) film (red open squares) agree with corresponding data of the 4ML/W(110) film (blue open circles). Likewise the standing wave dispersion of the 3MLCo/Cu(111) film roughly agrees with the standing wave dispersion of the 5ML/W(110) film [Fig. 12(b)]. The standing waves of the 4ML and 5ML films on Cu(111) (red open squares and red solid diamonds) finally agree approximately with the standing wave data of the 6ML/W(110) film [Fig. 12(c)].

V. COBALT ON Au(111)

Nucleation of the cobalt films begins at the elbows of the herringbone reconstruction with islands of two cobalt layers height [39]. The islands grow primarily in size rather than in thickness so that merely half the surface is covered by cobalt at 1ML nominal coverage [61]. The islands remain separate at even higher coverages because of the mismatch between distances of the nucleation centers and the cobalt lattice [62]. Even 6ML films display a rather regular arrangement of noncoalesced islands. The open structure of the cobalt film on

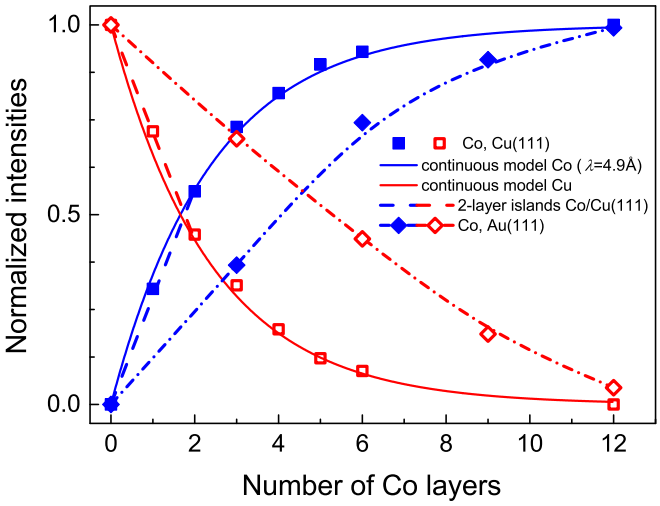

FIG. 13. (Color online) Normalized intensities of the low-energy Auger lines of cobalt (57 eV), copper (66 eV), and gold (74 eV) as function of the nominal cobalt coverage in monolayers. For cobalt on Cu(111) the cobalt intensity (blue solid squares) rises and the copper intensity (open red squares) decays approximately according to a layer-by-layer growth mode (blue and red solid lines). An even better agreement between modeling and the data is obtained if one takes the initial double island growth into account (blue and red dashed lines). On the Au(111) surface the rise of the cobalt signal and the decay of the gold signal (open red diamonds) is nearly linear up to high nominal coverages indicating granular growth.

Au(111) is reflected in the intensities of the low-energy Auger lines. Figure 13 shows the intensities of the cobalt and gold Auger lines as solid blue diamonds and open red diamonds, respectively. The intensities are normalized to their maximum value at zero cobalt coverage and at 12ML coverage, for gold and cobalt respectively. The rise of the cobalt intensity and the decay of the gold intensity are nearly linear up to high coverage indicating granular growth.

For cobalt on copper, on the other hand, the experimental data are approximately described by a continuous growth model:

$$I_{\mathrm{norm},Co} = 1 - \exp\left(-\frac{N d_{\mathrm{mono}}}{\lambda}\right), \tag{6}$$

$$I_{\mathrm{norm},Cu} = \exp\left(-\frac{N d_{\mathrm{mono}}}{\lambda}\right). \tag{7}$$

Here, N is the number of cobalt layers, d_{mono} the thickness of one cobalt layer, and $\lambda = 4.9$ Å the mean-free path in cobalt at 57 eV (solid lines in Fig. 13). A better agreement with the data is achieved if the initial growth in form of double-layer islands is considered (dashed lines).

The granular structure of the cobalt films on Au(111) gives rise to large diffuse elastic scattering, preventing a study of standing spin waves at low wave vectors. We therefore focus on wave vectors $q_{\parallel} > 0.5$ Å^{-1} where we found intense spin wave signals. Figure 14 compares the spin wave spectra at $q_{\parallel} = 0.6$ Å^{-1} for 6ML cobalt films deposited on Au(111), Cu(111), and W(110). The spectral response of all three films peaks at about the same energy, however, it is considerably broader

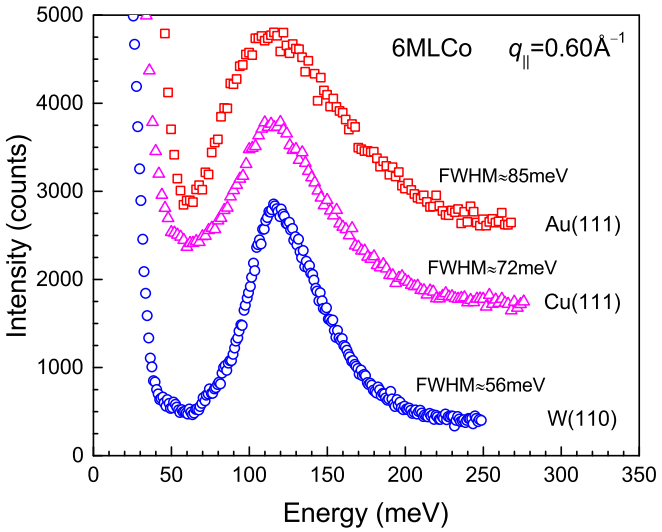

FIG. 14. (Color online) Comparison of the spin wave spectra of 6ML Co on Au(111), Cu(111), and W(110) for a wave vector of $q_{\parallel} = 0.6\,\text{Å}^{-1}$. The energy losses peak at the same energy. The width increases however from W(110) to Au(111) because of kinematic broadening.

on the Au(111) surface. In the following we show that the broadening is entirely due to kinematic broadening resulting from the diffuse scattering, which entails that a larger $q_{\parallel}$ space is sampled.

For a quantitative analysis of the kinematic broadening we first consider the intensity of the specular reflected beam of cobalt films as function of the angle of the reflected beam $\theta^{(\text{f})}$. The angle $\theta^{(\text{f})}$ is converted into the momentum transfer $\Delta K_{||} = k^{(\text{f})}\sin(\theta^{(\text{f})}) - k^{(\text{i})}\sin(\theta^{(\text{i})})$. The data are displayed in Fig. 15. For the 5ML cobalt film on W(110) the intensity has the form of a Gaussian in the center with Lorentzian-like tails on both sides (black squares in Fig. 15). By using the electron optical calculations described in Ref. [21] one can

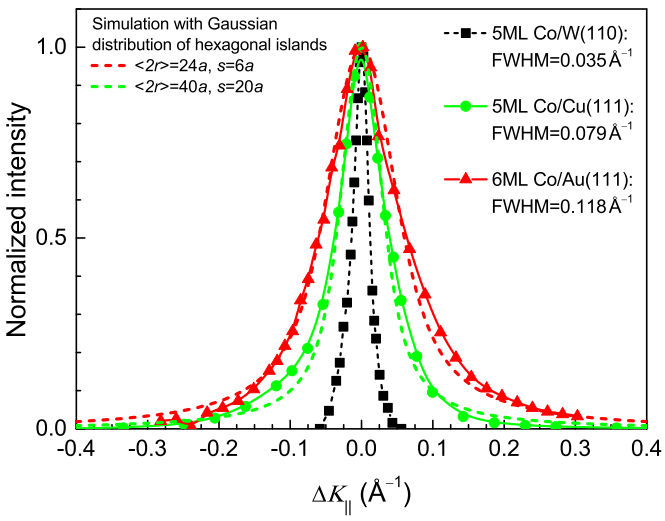

FIG. 15. (Color online) Normalized intensity of the specular reflected beam versus $\Delta K_{\parallel}$ of cobalt films deposited on Au(111), Cu(111), and W(110) (red triangles, green circles, and black squares, respectively, see text for discussion).

TABLE I. From left to right the table shows the substrate used, the FWHM of the spectra, the FWHM of the elastic peaks, the FWHM after unfolding the spectrum [Eq. (9)], the kinematic broadening $\Delta\hbar\omega$, and the resulting intrinsic FWHM of the spin wave signal.

Substrate	FWHM energy loss	FWHM elastic peak	FWHM real	$\Delta\hbar\omega$ kinematic	FWHM intrinsic
W(110)	56 meV	15 meV	52 meV	11 meV	41 meV
Cu(111)	72 meV	23 meV	64 meV	24 meV	40 meV
Au(111)	85 meV	26 meV	77 meV	36 meV	41 meV

show that width and shape are entirely determined by the acceptance angle of the lens system in that case. On the Cu(111) and Au(111) substrates, the momentum widths of the specular beams are considerably larger (green circles and red triangles respectively). Moreover, the shape of the curves resembles a Lorentzian (dashed lines). Simulations show that the Lorentzian form results from the incoherent superposition of the scattering from an ensemble of islands with a Gaussian (i.e., random) size distribution. For simplicity the islands were assumed to be of hexagonal shape both for the cobalt islands on Au(111) and on Cu(111) [in reality the islands are triangular on Cu(111)]. Best fit to the experimental data is obtained for islands with mean diameters of 40 and 24 atoms and a standard deviation of 20 and 6 atoms, for Cu(111) and Au(111) respectively. The resulting mean sizes are in excellent agreement with the island sizes observed in STM images [31,39]. We therefore conclude that the broad quasi-Lorentzian shape of specular reflected beam results from the morphology of the cobalt films.

Because of the diffuse elastic scattering on Cu(111) and Au(111) the spin wave spectra probe a larger range of $q_{\parallel}$ values than on the W(110) surface, namely $\Delta q_{\parallel} = 0.079\,\text{Å}^{-1}$ and $\Delta q_{\parallel} = 0.118\,\text{Å}^{-1}$ for the Cu(111) and Au(111) substrates, respectively. The wider $q_{\parallel}$-range results in an energy broadening according to

$$\Delta\hbar\omega \cong \frac{\partial\hbar\omega(q_{\parallel})}{\partial q_{\parallel}}\Delta q_{\parallel}. \tag{8}$$

With the dispersion $\partial\hbar\omega/\partial q_{||} = 303\,\text{meVÅ}$ at $q_{\parallel} = 0.6\,\text{Å}^{-1}$ a kinematic energy broadening of 11 meV, 24 meV, and 36 meV is calculated for the cobalt films on W(110), Cu(111), and Au(111) substrates, respectively (fifth column in Table I). In order to obtain the intrinsic FWHM of the spin wave signal, the experimentally observed FWHM needs to be corrected for the energy resolution of the experiment as indicated by the FWHM of the elastic peak (third column in Table I). To do that, we note that the ratio of true width of the spin wave energy loss ($\text{FWHM}_{\text{real}}$) to the width of the Voigt function ($\text{FWHM}_{\text{Voigt}}$) representing the convolution of spin wave signal and the resolution function depends only on the ratio of the width the Voigt function ($\text{FWHM}_{\text{Voigt}}$) to the width of the resolution function (FWHM_{el}). We have calculated numerically a large number of convolutions for $1.2 < \text{FWHM}_{\text{Voigt}}/\text{FWHM}_{\text{el}} < 10$. The results are excellently described by

$$\frac{\text{FWHM}_{\text{real}}}{\text{FWHM}_{\text{Voigt}}} \approx 1 - 5628\exp\left[-8.656\left(\frac{\text{FWHM}_{\text{Voigt}}}{\text{FWHM}_{\text{el}}}\right)^{0.2}\right]. \tag{9}$$

Using this approximation the values in the fourth column of Table I are obtained. The finally resulting intrinsic FWHM of the spin wave signal, as listed in the last column of Table I, agree within the limit of error.

In summary we conclude that the spin wave spectral densities of 6ML cobalt layers on the three different substrates agree both in peak energy and in their intrinsic width. We note that the spectral response at $q_{\parallel} = 0.6\,\text{Å}^{-1}$ stems from more than one mode (Sec. III). Hence, the true FWHM of the individual spin wave modes at $q_{\parallel} = 0.6\,\text{Å}^{-1}$ is smaller than 40 meV.

VI. DISCUSSION

A. Effects of film morphology on the spin wave spectra

Except for the kinematic broadening discussed above, the island morphology has no noticeable effect on the spin wave spectra for larger $q_{\parallel}$ values. The same can be said for the acoustic mode at low $q_{\parallel}$ values inasmuch as experimental data are available, which is the case for cobalt on Cu(111). Figures 10 and 12 show that the data points for the acoustic mode for films on W(110) and Cu(111) fall on top of each other. Hence there is no noticeable effect of the finite size of the islands on the measured dispersion. This is not so surprising; however, boundary conditions at the island edges are expected to become important when the lateral dimensions of the islands are comparable to the wavelength of the spin wave. For cobalt on Cu(111) this would be the case for wave vectors $q_{\parallel}$ smaller than $0.05\,\text{Å}^{-1}$, which is out of the realm of our investigation. We further note that the fcc structure of the thin cobalt films on Cu(111) has apparently no significant effect on the energies of the acoustic mode. This is presumably because nearest- and next-nearest-neighbor interactions dominate the spin wave energies and their distances are the same for the fcc and hcp structure.

The result for the submonolayer coverage of 0.7ML [Fig. 12(a)] requires extra consideration. For submonolayer coverage, cobalt assembles in two-atom-high islands of triangular shape. This double-layer structure is responsible for the fact that the Curie temperature for these islands is above 300 K so that spin waves exist at room temperature. From the nucleation density observed in STM images [34,35,63,64] one calculates a mean island size of ∼1900 atoms for the nominal 0.7ML deposit, equivalent to a side length of the islands of about 50 atoms. These islands are large enough to sustain spin waves of wave vectors larger than the lower limit of wave vectors accessible to us. Possible different magnetic properties of the island edge atom as indicated by the reversed polarization of the edge atoms seen in spin-polarized scanning tunneling microscopy (STM) [65,66] should not have a significant effect on the spin wave spectra.

While there is no noticeable effect on the acoustic mode, the island morphology has drastic consequences for the standing spin waves of cobalt films deposited on Cu(111). The standing wave energy of nominal 2ML and 3ML films on Cu(111) coincide with the standing wave energies of 4ML and 5ML films on W(110) [Figs. 12(a) and 12(b)]. The data for the 5ML film on Cu(111) coincides with the 6ML film on W(110) for the same nominal thickness [Fig. 12(c)]. This agreement includes the data on the second standing wave.

The comparison of the standing spin wave data of films deposited on Cu(111) and W(110) suggest that the actual film thickness on copper is higher than the mean thickness. The enhanced height is a consequence of the initial growth in the form of twinned bilayer islands with bottom layer cobalt atoms occupying crystallographic different threefold hollow sites on Cu(111) (A and B sites, if the top copper layer atoms sit in C-type sites). The orientational domain boundaries impede the coalescence of the islands during subsequent growth of the Co film. A 5ML film on Cu(111), for example, is composed of flat-top islands with lateral sizes of 100–150 Å (Fig. 3 of Ref. [31]) with trenches between the islands. The trenches amount to about 25% of the imaged surface. De la Figuera *et al.* suggested that the trenches may reach down to the copper surfaces [31]. If that were true the mean height of the islands of a nominal 5ML film would be 6.7ML. The rapid decay of the Cu 66eV Auger line with coverage (Fig. 13), however, shows that even in the trenches the copper surface must at least be partially covered with cobalt. Hence the actual height of the islands of the nominal 5ML film should be higher than 5ML but lower than 6.7ML. The good agreement of the 5ML/Cu(111) data with the 6ML/W(110) data has thus a simple explanation.

For very thin films the spin wave data shows an equivalency of 2ML/Cu(111) and 4ML/W(110) films. Whether the island growth can also explain this result is debatable. According to STM images the average island height for a nominal coverage of 2ML on Cu(111) is 3ML, not 4ML (Fig. 1(d) of Ref. [67]). However, a small fraction of the surface also shows 4ML high islands. The standing wave signal of the 2ML film is rather weak (Fig. 11). It is therefore possible that the dispersion data assigned to the nominal 2ML film on Cu(111) actually stem from the 4ML patches. That assignment would entail that the majority of 3ML high islands does not produce visible standing waves, which is consistent with their absence in case of 3ML films on W(110). On the other hand one cannot *a priori* exclude the possibility that the standing waves observed for nominal 2ML films on Cu(111) actually stem from the 3ML islands. The 3ML islands on Cu(111) grow as fcc rather than hcp, which may lead to softer standing waves. Furthermore, the copper substrate may cause a softening of the exchange coupling at the interface compared to a tungsten substrate. Only theory can resolve this issue.

B. Comparison to fcc (100) cobalt films

We now compare the spin wave spectrum of fcc Co(001) films grown on Cu(100) [23] with the hcp Co(0001) films grown on W(110) for the same thickness layers. Figure 16 shows the experimental data for 5ML films along the $\overline{\Gamma\,\text{X}}$ direction for the fcc film and along the $\overline{\Gamma\,\text{K}}$ direction for the hcp film. Data for the fcc films are depicted as solid red circles and squares for the acoustic and standing mode, respectively. Data for the hcp films are represented by open blue circles and squares for the acoustic mode and the first standing mode, respectively.

The acoustic modes of fcc and hcp films agree with each other for low $q_{\parallel}$. This result is consistent with the predictions of the nearest-neighbor Heisenberg model with a single, layer-independent exchange constant (1NN-model). In that model

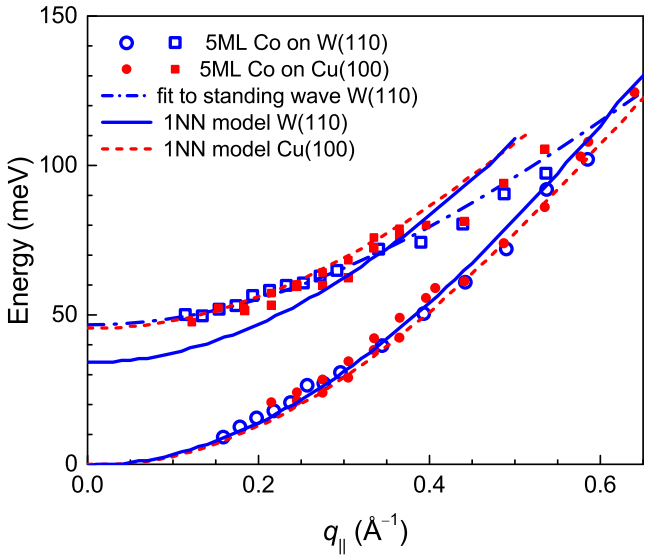

FIG. 16. (Color online) Comparison of the dispersion of 5ML hcp Co(0001) films on W(110) (blue open symbols) and fcc Co(100) films on Cu(100) (red solid symbols) along the $\overline{\Gamma\,\mathrm{K}}$ and $\overline{\Gamma\,\mathrm{X}}$ directions of the Brillouin, respectively. The solid and dashed lines are calculated within the nearest-neighbor Heisenberg model with $J = 15$ meV for hcp and fcc films, respectively. The dash-dotted line is a fit to the experimental data on W(110) as described earlier.

the dispersion of the lowest energy mode is

$$\hbar\omega_{\mathrm{acoustic}} = \tfrac{16}{3} JS\{3 - \cos(q_{||}a_0) - 2\cos(q_{||}a_0/2)\}$$
$$\approx 4JSa_0^2q_{||}^2 \quad \text{for} \quad a_0^2q_{||}^2 \ll 1 \qquad (10)$$

for the hcp film along the $\overline{\Gamma\,\mathrm{K}}$ direction and

$$\hbar\omega_{\mathrm{acoustic}} = 8JS\{1 - \cos(q_{||}a_0)\}$$
$$\approx 4JSa_0^2q_{||}^2 \quad \text{for} \quad a_0^2q_{||}^2 \ll 1 \qquad (11)$$

for the fcc film along the $\overline{\Gamma\,\mathrm{X}}$ direction. Since there is little deviation in the nearest-neighbor distances between fcc and hcp the exchange coupling JS should also be rather similar, and thus the dispersion in the acoustic limit. For larger $q_{\parallel}$ values the dispersion curves of the acoustic mode for the two films slightly deviate from each other for the same exchange constant $J = 15$ meV (solid lines in Fig. 16).

What is surprising is the fact that the standing wave energies for the fcc and hcp film are nearly identical. In the limit $q_{\parallel} = 0$, the spin precession amplitude is uniform within a layer and differs merely from one layer to the next. The energy of a standing mode at $q_{\parallel} = 0$ is therefore entirely determined by the interlayer exchange coupling. The number of nearest-neighbor interlayer interactions is four and three for the fcc and hcp film, respectively. Thus one would expect a frequency ratio of the standing mode energy of 4/3, at variance with the experimental result (Fig. 16). A possible explanation could lie in the contribution of next-nearest neighbors. Films with hcp structure possess three next-nearest interlayer neighbors whereas fcc films have only one interlayer next-nearest neighbor. It is therefore conceivable that the larger number of next-nearest neighbors in hcp films compensates for the lesser number of nearest neighbors. This statement entails that the nearest-neighbor Heisenberg model (1NN model) with uniform exchange coupling constants fails to describe the dispersion curves of the hcp films. The solid and dashed lines in Fig. 16 show the dispersion curves calculated for the acoustic and first standing mode respectively ($J = 15$ meV). As expected, the ratio of the standing mode energies for the fcc and hcp films is 4/3 at $q_{\parallel} = 0$. Only the standing wave of the fcc film is well described by the 1NN model. We remark, however, that the agreement in case of the fcc films is fortuitous to some extent. The reasons have been discussed in Ref. [23]. In reality, the exchange coupling constants in fcc films depend heavily on the proximity of the layer to the surface or to the interface with the substrate. Furthermore, interlayer and intralayer exchange coupling constants differ from each other, in particular near the surface or the interface.

VII. CONCLUSIONS

As was shown previously for fcc cobalt films on Cu(100), the analysis of the spectrum of standing spin waves as a function of the layer thickness in combination with a theoretical study reveals information on the layer dependence of the exchange coupling [23]. It was our aim to lay the experimental foundation for an extension of the method to hcp layers. To achieve this objective we have studied cobalt films deposited onto three different substrates, W(110), Cu(111), and Au(111). Only the films deposited on W(110) and Cu(111) are of sufficient quality to support well-defined standing spin waves. For a theoretical analysis of the data the small $(1x1)$ unit cell of the cobalt films on Cu(111) is attractive. We found however that an assignment of a particular standing wave dispersion curve to a film thickness is not possible *a priori* because of the granular structure of the film. By comparison to (flat) cobalt films on W(110) we could attribute the standing wave of the nominal 5ML film on Cu(111) to a film of an actual local thickness of 6ML. This assignment is reasonable in view of the STM images of nominal 5ML films [31], as discussed before. The standing wave energies of thinner films on Cu(111) may possibly also be explained by the island growth. However, one can not exclude the possibility that the fcc (111) structure of very thin films on Cu(111) results in a softening of the interlayer exchange coupling.

There is therefore a need for theoretical studies in several directions. First, 5ML hcp cobalt films in 1×1 structure deposited on Cu(111) should be investigated to see whether one may achieve agreement with the experimental data. From there one could proceed to 2–3ML films, both in hcp and fcc structure. The outcome of such a study could be that one could assign standing wave dispersion curves to particular island thicknesses. Because of the defined film thicknesses the hcp films on W(110) may be most promising for a theoretical analysis of the standing spin wave spectrum as function of the film thickness, despite the large unit cell. Such a study using a using $(10x1)$ unit cell is a subject for future work [68].

ACKNOWLEDGMENTS

The authors gratefully acknowledge in-depth discussions with Arthur Ernst, Samir Lounis, Manuel Dos Santos Dias, Flaviano Dos Santos, and Antonio Costa. The able technical assistance of Bernd Küpper has been instrumental to the success of this work.

[1] C. M. Schneider and J. Kirschner, in *Handbook of Surface Science* 2, edited by K. Horn, and M. Scheffler (Elsevier, Amsterdam, 2000).

[2] C. A. F. Vaz, J. A. C. Bland, and G. Lauhoff, Rep. Prog. Phys. **71**, 056501 (2008).

[3] D. L. Mills, in *Ultrathin Magnetic Structures*, edited by J. A. C. Bland, and B. Heinrich (Springer, Berlin, 1994), p. 91.

[4] M. Farle, W. Platow, A. N. Anisimov, P. Poulopoulos, and K. Baberschke, Phys. Rev. B **56**, 5100 (1997).

[5] G. Chen *et al.*, Phys. Rev. Lett. **110**, 177204 (2013).

[6] D. L. Mills, J. Phys. Chem. Solids **28**, 2245 (1967).

[7] H. Ibach and D. L. Mills, *Electron Energy Loss Spectroscopy and Surface Vibrations* (Academic Press, New York, 1982).

[8] H. Ibach, D. Bruchmann, R. Vollmer, M. Etzkorn, P. S. A. Kumar, and J. Kirschner, Rev. Sci. Instrum. **74**, 4089 (2003).

[9] R. Vollmer, M. Etzkorn, P. S. Anil Kumar, H. Ibach, and J. Kirschner, Phys. Rev. Lett. **91**, 147201 (2003).

[10] H. Ibach, Surf. Sci. **630**, 301 (2014).

[11] A. T. Costa, R. B. Muniz, and D. L. Mills, Phys. Rev. B **69**, 064413 (2004).

[12] M. Etzkorn, Ph.D. thesis, Martin-Luther University Halle-Wittenberg, 2005.

[13] M. Etzkorn, P. S. Anil Kumar, W. Tang, Y. Zhang, and J. Kirschner, Phys. Rev. B **72**, 184420 (2005).

[14] M. Etzkorn, P. S. Anil Kumar, R. Vollmer, H. Ibach, and J. Kirschner, Surf. Sci. **566–568**, 241 (2004).

[15] R. Vollmer, M. Etzkorn, P. S. A. Kumar, H. Ibach, and J. Kirschner, Thin Solid Films **464–465**, 42 (2004).

[16] C. L. Gao, A. Ernst, G. Fischer, W. Hergert, P. Bruno, W. Wulfhekel, and J. Kirschner, Phys. Rev. Lett. **101**, 167201 (2008).

[17] T. Balashov, A. F. Takács, M. Däne, A. Ernst, P. Bruno, and W. Wulfhekel, Phys. Rev. B **78**, 174404 (2008).

[18] W. Wulfhekel and S. Blügel, Surf. Sci. **630**, 300 (2014).

[19] T. Balashov, P. Buczek, L. Sandratskii, A. Ernst, and W. Wulfhekel, J. Phys.: Condens. Matter **26**, 394007 (2014).

[20] H. Ibach, J. Rajeswari, and C. M. Schneider, Rev. Sci. Instrum. **82**, 123904 (2011).

[21] H. Ibach and J. Rajeswari, J. Electr. Spectros. Rel. Phenom. **185**, 61 (2012).

[22] J. Rajeswari, H. Ibach, C. M. Schneider, A. T. Costa, D. L. R. Santos, and D. L. Mills, Phys. Rev. B **86**, 165436 (2012).

[23] J. Rajeswari, H. Ibach, and C. M. Schneider, Phys. Rev. Lett. **112**, 127202 (2014).

[24] L. Bergqvist, A. Taroni, A. Bergman, C. Etz, and O. Eriksson, Phys. Rev. B **87**, 144401 (2013).

[25] K. Zakeri, Phys. Rep. **545**, 47 (2014).

[26] Y. Zhang, P. Buczek, L. Sandratskii, W. X. Tang, J. Prokop, I. Tudosa, T. R. F. Peixoto, K. Zakeri, and J. Kirschner, Phys. Rev. B **81**, 094438 (2010).

[27] A. T. Costa, R. B. Muniz, and D. L. Mills, Phys. Rev. B **70**, 054406 (2004).

[28] H. Fritzsche, J. Kohlhepp, and U. Gradmann, Phys. Rev. B **51**, 15933 (1995).

[29] H. Knoppe and E. Bauer, Phys. Rev. B **48**, 1794 (1993).

[30] N. N. Negulyaev, V. S. Stepanyuk, P. Bruno, L. Diekhöner, P. Wahl, and K. Kern, Phys. Rev. B **77**, 125437 (2008).

[31] J. de la Figuera, J. E. Prieto, C. Ocal, and R. Miranda, Phys. Rev. B **47**, 13043 (1993).

[32] L. Diekhoner, M. A. Schneider, A. N. Baranov, V. S. Stepanyuk, P. Bruno, and K. Kern, Phys. Rev. Lett. **90**, 236801 (2003).

[33] T. Balashov, T. Schuh, A. F. Takécs *et al.*, Phys. Rev. Lett. **102**, 257203 (2009).

[34] S. Ouazi, S. Wedekind, G. Rodary, H. Oka, D. Sander, and J. Kirschner, Phys. Rev. Lett. **108**, 107206 (2012).

[35] D. Sander, S.-H. Phark, M. Corbetta, J. A. Fischer, H. Oka, and J. Kirschner, J. Phys.: Condens. Matter **26**, 394008 (2014).

[36] M. Ø. Pedersen, I. A. Bönicke, E. Laegsgaard, I. Stensgaard, A. Ruban, J. K. Nørskov, and F. Besenbacher, Surf. Sci. **387**, 86 (1997).

[37] S. Mülller, G. Kostka, T. Schäfer, J. de la Figuera, J. E. Prieto, C. Ocal, R. Miranda, K. Heinz, and K. Müller, Surf. Sci. **352–354**, 46 (1996).

[38] C. Rath, J. E. Prieto, S. Müller, R. Miranda, and K. Heinz, Phys. Rev. B **55**, 10791 (1997).

[39] B. Voigtländer, G. Meyer, and N. M. Amer, Phys. Rev. B **44**, 10354 (1991).

[40] R. Allenspach, M. Stampanoni, and A. Bischof, Phys. Rev. Lett. **65**, 3344 (1990).

[41] T. Duden and E. Bauer, Proc. Mat. Res. Soc. **475**, 283 (1997).

[42] M. Speckmann, H. P. Oepen, and H. Ibach, Phys. Rev. Lett. **75**, 2035 (1995).

[43] C. Dupas, P. Beauvillain, C. Chappert, J. P. Renard, F. Trigui, P. Veillet, E. Velu, and D. Renard, J. Appl. Phys. **67**, 5680 (1990).

[44] C. H. Lee, H. He, F. J. Lamelas, W. Vavra, C. Uher, and R. Clarke, Phys. Rev. B **42**, 1066 (1990).

[45] T. Moriya, Phys. Rev. **120**, 91 (1960).

[46] J.-H. Moon, S.-M. Seo, K.-J. Lee, K.-W. Kim, J. Ryu, H.-W. Lee, R. D. McMichael, and M. D. Stiles, Phys. Rev. B **88**, 184404 (2013).

[47] K. Zakeri, Y. Zhang, J. Prokop, T.-H. Chaung, N. Sakr, W. X. Tang, and J. Kirschner, Phys. Rev. Lett. **104**, 137203 (2010).

[48] P. Buczek, A. Ernst, and L. M. Sandratskii, Phys. Rev. Lett. **105**, 097205 (2010).

[49] E. Michel, H. Ibach, and C. M. Schneider (unpublished).

[50] M. Pratzer, H. J. Elmers, and M. Getzlaff, Phys. Rev. B **67**, 153405 (2003).

[51] M. J. Verstraete, J. Phys.: Condens. Matter **25**, 136001 (2013).

[52] See Supplemental Material at http://link.aps.org/supplemental/10.1103/PhysRevB.92.024407 for comparison of the measured dispersion of the modes assigned to phonons with theoretical calculations.

[53] T. Duden, R. Zdyb, M. S. Altman, and E. Bauer, Surf. Sci. **480**, 145 (2001).

[54] J. Rajeswari, E. Michel, H. Ibach, and C. M. Schneider, Phys. Rev. B **89**, 075438 (2014).

[55] B. M. Hall, S. Y. Tong, and D. L. Mills, Phys. Rev. Lett. **50**, 1277 (1983).

[56] C. H. Li, S. Y. Tong, and D. L. Mills, Phys. Rev. B **21**, 3057 (1980).

[57] S. Y. Tong, C. H. Li, and D. L. Mills, Phys. Rev. Lett. **44**, 407 (1980).

[58] M. Balden, S. Lehwald, H. Ibach, A. Ormeci, and D. L. Mills, J. Electron Spectros. Rel. Phen. **64-65**, 739 (1993).

[59] M. Balden, S. Lehwald, and H. Ibach, Phys. Rev. B **53**, 7479 (1996).

[60] Y. Zhang, T.-H. Chuang, K. Zakeri, and J. Kirschner, Phys. Rev. Lett. **109**, 087203 (2012).

[61] R. Belkhou, N. Marsot, H. Magnan, L. Fèvre, N. T. Barrett, C. Guillot, and D. Chandesris, J. Electron Spectros. Rel. Phen. **101–103**, 251 (1999).
[62] P. M.-M. S. Padovani, F. Scheurer, J. P. Bucher, Appl. Phys. A **66**, 1199 (1998).
[63] J. de la Figuera, J. E. Prieto, C. Ocal, and R. Miranda, Surf. Sci. **307–309**, Part A, 538 (1994).
[64] J. de la Figuera, J. E. Prieto, G. Kostka, S. Müller, C. Ocal, R. Miranda, and K. Heinz, Surf. Sci. **349**, L139 (1996).
[65] O. Pietzsch, A. Kubetzka, M. Bode, and R. Wiesendanger, Phys. Rev. Lett. **92**, 057202 (2004).
[66] H. Oka, K. Tao, S. Wedekind, G. Rodary, V. S. Stepanyuk, D. Sander, and J. Kirschner, Phys. Rev. Lett. **107**, 187201 (2011).
[67] J. E. Prieto, J. de la Figuera, and R. Miranda, Phys. Rev. B **62**, 2126 (2000).
[68] F. Santos and S. Lounis (private communication).